Article

Investigation of Chaboche and Bouc–Wen Parameters of Quenched and Tempered Steel and Comparison of Model Predictive Capabilities

Ciro Santus [1], Lorenzo Romanelli [1,*], Tommaso Grossi [1], Leonardo Bertini [1], Paolo Neri [1], Luca Le Bone [2], Francesco Chiesi [2] and Leonardo Tognarelli [2]

[1] Department of Civil and Industrial Engineering—DICI, University of Pisa, Largo Lucio Lazzarino 1, 56122 Pisa, Italy

[2] Baker Hughes—Nuovo Pignone, Via Felice Matteucci 2, 50127 Florence, Italy

[*] Correspondence: lorenzo.romanelli@phd.unipi.it

Abstract: The aim of this paper is to model the elastic–plastic uniaxial behaviour of a quenched and tempered steel. The common Chaboche isotropic kinematic hardening model (CIKH) is introduced, and a physics-based procedure is proposed to determine its parameters. This procedure is based on strain- and stress-controlled tests and is focused on the stabilized cycles. The imposed cycle properties are the hysteresis area, the stress range, the slope at the inversion points, obtained from the stabilized cycles of strain-controlled tests, and the ratcheting rate extracted from a stress-controlled test. The novelty of the algorithm is to determine the hardening parameters from the global properties of the cycle rather than imposing a pointwise fitting, which is also implemented to calculate the parameters for a comparison. The Bouc–Wen model showed great flexibility in describing nonlinear behaviours, corresponding to different physical phenomena, through an appropriate tuning of its parameter values. In this paper, another optimization approach is developed to estimate the Bouc–Wen coefficients and accurately describe the same experimental cycles. The performances of the Bouc–Wen model are compared with the predictions of the Chaboche model, and a discussion comparing the techniques used to reproduce cyclic plastic behaviour is provided.

Keywords: cyclic plasticity; kinematic hardening; closed-form expressions; numerical algorithms; nonlinear hysteretic behaviour

1. Introduction

An accurate description of the effect of plastic strain on the mechanical behaviour of materials is necessary for a reliable prediction of the mechanical response beyond the elastic limit. There are many industrial applications in which plasticity plays a fundamental role, such as contact mechanics [1], fatigue analysis [2] and residual stresses' analysis [3]. In our previous paper, Ref. [4], it is evident that, without considering plasticity around the notch, the stress predictions could reach very high values, which are approximately similar to the ultimate stress of the material and not meaningful for cyclic loading analysis. The Chaboche kinematic hardening (CKH) model is a powerful constitutive law to model the plasticity of metals. It was introduced by Chaboche [5], extending the Armstrong and Frederick model [6] by adding multiple backstress components with different properties. It can also be efficiently combined with the isotropic hardening rule proposed by Voce [7], as in Refs. [8–10], and both hardening rules are implemented in Ansys commercial finite element software [11]. The combination of a CKH model and Voce isotropic hardening model results in the Chaboche isotropic kinematic hardening (CIKH) model. The CKH model has often been involved in fatigue analyses, as in [12–14]. In these papers, the theory of critical distances and the strain energy density criterion, which are efficient tools for predicting the fatigue life of components, were used, combined with the CKH model

showing better predictions rather than maintaining a simple, linear, elastic behaviour. This model was also employed in contact mechanics problems, as in Ref. [15].

In recent years, researchers made some modifications to the original formulation of the CIKH model, as in [16,17]. In this latter paper, a refinement was proposed to properly model the ratcheting rate, then elaborated in [18]. A backstress with a threshold was introduced. Below this threshold the backstress behaves according to linear Prager rule, while it behaves like Chaboche nonlinear hardening model above the threshold. The concept of the backstress with threshold was extended in [19] to model both the ratcheting rate and the mean stress relaxation. Alternatively, to properly model the ratcheting rate, in Ref. [20] a multiplicative hardening rule was introduced, in which one of the two coefficients of some backstress components is a function of another dimensionless, second-order, internal variable that nonlinearly evolves as the backstress components of the CIKH model. This approach was applied to model the cyclic plastic behaviour of Steel 316 L and Carbon Steel 1026 in [20], and was then extended to aluminium alloy 7075-T6 in [21,22], and to Ti-6Al-4V in [23]. The CKH model is generally combined with the Von Mises yielding law but, in [24], it was employed together with the Hill yielding law for anisotropic metals [25]; for example, to model the cyclic plastic behaviour of Maraging 300, obtained through additive manufacturing technologies.

In principle, the stabilized cycles of strain-controlled tests alone can be engaged to determine the parameters. However, if the transient of the stress-controlled test plays a fundamental role in further analyses, the ratcheting rate must also be considered. In [26,27], the ratcheting rate was employed to calculate the parameters, whereas in [28,29] both uni-axial stress-controlled tests and strain-controlled tests were exploited. The algorithms used to calculate these parameters can follow different approaches, such as genetic algorithms, as in [30,31], particle swarm optimization in [32], and the differential evolution algorithm in [33]. All of these techniques require a great computational effort.

Alternatively, the Bouc–Wen (B-W) model [34,35] is widely used to replicate the hysteretic behaviours of systems such as wire rope isolators [36], piezoelectric actuators [37] and seismic isolation in [38]. Given the widespread diffusion of this model, the development of identification procedures that can relate B-W parameters to the experimental data are crucial. In [39], dynamic tests were developed to characterize wire rope isolators, and then the Levenberg–Marquardt (L-M) algorithm [40,41] was engaged to obtain the parameters. In [42], a novel method of attenuating vibration using vacuum-packed particles as the materials responsible for energy dissipation was investigated and a genetic algorithm was performed; in [43], the vibratory behaviour of a full-scale steel cantilever beam was studied and a hybrid evolutionary algorithm, which utilized selected stochastic operators, heuristics and problem-specific information, was involved.

In this manuscript, a novel procedure to calculate CIKH model parameters was exploited. The procedure was carried out on three strain-controlled tests and one stress-controlled test. The cycle properties that were imposed were the hysteresis area, the stress range, the slope at the inversion points, the average stress and the average plastic strain. These were all extracted from the stabilized cycles of strain-controlled tests, and the ratcheting rate extracted from the stress-controlled test. This can be motivated considering that a good prediction of the global properties of the stabilized cycle is generally sufficient in fatigue analyses. Multiaxial fatigue criteria, in fact, generally require global quantities of the stabilized cycle to be applied. Once the CKH model parameters were obtained, the model was also refined with the introduction of a fourth backstress and then the Voce isotropic hardening law. In addition to this, the determination of CKH model parameters was conducted by using a classical pointwise fitting between the experimental data and the modeled curve. In addition, a B-W model was engaged to reproduce cyclic loadings. Cyclic plasticity is a nonlinear hysteretic behaviour, and therefore pertinent to the range of application of the B-W model. The parameters were computed using the L-M algorithm, as proposed in [44].

Section 2 is dedicated to explaining the theoretical background of the CIKH model and B-W model. In Section 3, the experimental data employed in this work are presented, and the proposed procedure to calculate CIKH model parameters, together with the algorithm used to determine Bouc–Wen constants, are formalized. In Section 4, the results of the calibration techniques are exposed. The results obtained with a classical pointwise fitting are initially shown. The results according to the proposed procedure are then presented, and, finally, the results obtained using Bouc–Wen are reported. In Section 5, a discussion and comparison between the three approaches are provided, together with suggestions for future studies about the modeling of cyclic plastic behaviour.

2. Theoretical Background

2.1. Mathematical Formalization of CKH Model

In this paragraph, the aim is to derive the differential equation about the CKH model for a uniaxial loading case, according to [4]. In a plain specimen under uniaxial stress, the stress tensor is given by (1), where x indicates the loading direction.

$$\mathbf{S} = \begin{pmatrix} \sigma_{xx} & 0 & 0 \\ 0 & 0 & 0 \\ 0 & 0 & 0 \end{pmatrix} \tag{1}$$

The total strain tensor is obtained by adding the plastic strain tensor and the elastic strain tensor, as in Equation (2).

$$\varepsilon^{\mathbf{tot}} = \varepsilon^{\mathbf{el}} + \varepsilon^{\mathbf{pl}} \tag{2}$$

When creating an elastic–plastic analysis, the first component is the yield law, which, in this case, is the common Von Mises yield criterion. The evolution of the yield surface according to this criterion is formalized in Equation (3).

$$\mathrm{F} = \sqrt{\frac{3}{2}(\mathbf{S_D} - \chi) : (\mathbf{S_D} - \chi)} - \sigma_{\mathrm{Y}} = 0 \tag{3}$$

In this latter equation, $\mathbf{S_D}$ is the deviatoric component of the stress tensor $\mathbf{S}$, σ_{Y} is the elastic limit of the material and χ is the backstress tensor. The second fundamental part is the plastic flow rule. Prandtl–Reuss is the plastic flow rule associated with the Von Mises yield function and is presented in Equation (4). This is not the only plastic flow rule suitable for an elastic–plastic analysis.

$$\begin{cases} \mathrm{d}\varepsilon_{xx}^{\mathrm{pl}} = \left[\sigma_{xx} - 0.5(\sigma_{yy} + \sigma_{zz})\right]\mathrm{d}\lambda \\ \mathrm{d}\varepsilon_{yy}^{\mathrm{pl}} = \left[\sigma_{yy} - 0.5(\sigma_{xx} + \sigma_{zz})\right]\mathrm{d}\lambda \\ \mathrm{d}\varepsilon_{zz}^{\mathrm{pl}} = \left[\sigma_{zz} - 0.5(\sigma_{xx} + \sigma_{yy})\right]\mathrm{d}\lambda \\ \mathrm{d}\varepsilon_{xy}^{\mathrm{pl}} = \frac{3}{2}\sigma_{xy}\mathrm{d}\lambda \\ \mathrm{d}\varepsilon_{xz}^{\mathrm{pl}} = \frac{3}{2}\sigma_{xz}\mathrm{d}\lambda \\ \mathrm{d}\varepsilon_{yz}^{\mathrm{pl}} = \frac{3}{2}\sigma_{yz}\mathrm{d}\lambda \end{cases} \tag{4}$$

The plastic flow rule allows for us to understand which of the plastic strain tensor components are not null, but it is not able to calculate their values, as $\mathrm{d}\lambda$ remains unknown in Equation (4). To accomplish this, it is necessary to introduce a hardening rule. The CKH model is described by the differential Equation (5):

$$\mathrm{d}\chi_i = \frac{2}{3}C_i\mathrm{d}\varepsilon^{\mathbf{pl}} - \gamma_i\chi_i\mathrm{d}p \tag{5}$$

In Equation (5), C_i and γ_i are the contants of the CKH model and $\mathrm{d}p$ is defined in Equation (6).

$$\mathrm{d}p = \sqrt{\frac{2}{3}\mathrm{d}\varepsilon^{\mathbf{pl}} : \mathrm{d}\varepsilon^{\mathbf{pl}}} \tag{6}$$

Focusing on only a plain specimen under uniaxial loading, the incremental plastic strain tensor is given in Equation (7), whereas the backstress tensor is reported in Equation (8) for each backstress component.

$$\mathrm{d}\varepsilon^{\mathbf{pl}} = \mathrm{d}\varepsilon^{\mathrm{pl}}_{xx}\begin{pmatrix} 1 & 0 & 0 \\ 0 & -0.5 & 0 \\ 0 & 0 & -0.5 \end{pmatrix} \tag{7}$$

$$\chi_i = \frac{2}{3}\chi_i\begin{pmatrix} 1 & 0 & 0 \\ 0 & -0.5 & 0 \\ 0 & 0 & -0.5 \end{pmatrix} \tag{8}$$

Equation (7) is consistent with the Prandtl–Reuss plastic flow rule, which states that the incremental plastic strain tensor and the deviatoric component of the stress tensor are parallel. Equation (8) provides the backstress tensor form used for each backstress component. After substituting Equations (1) and (8) into Equation (3), it is possible to obtain the relationship between the stress and the backstress for an uniaxial loading case (Equation (9)), where μ is equal to 1 during positive loading (tending-to-tensile stress), while it is equal to -1 during negative loading (tending to compression). In Equation (9), $\chi = \sum_{i=1}^{k}\chi_i$ and k indicate the number of backstress components that are considered.

$$\sigma_{xx} = \mu\sigma_0 + \chi \tag{9}$$

The backstress tensor for each component in Equation (8) is multiplied by the scalar factor $\frac{2}{3}$, and this last statement is justified by the fact that the yielding surface is translated in the deviatoric stress space, and omitting this term results in a scalar factor term in Equation (9). By substituting Equations (7) and (8) into Equation (5) and considering that, for an uniaxial loading case, $\mathrm{d}p = |\mathrm{d}\varepsilon^{\mathrm{pl}}_{xx}|$, Equation (10) provides a general representation of the evolution of each backstress component.

$$\frac{2}{3}\mathrm{d}\chi_i\begin{pmatrix} 1 & 0 & 0 \\ 0 & -0.5 & 0 \\ 0 & 0 & -0.5 \end{pmatrix} = \frac{2}{3}C_i\begin{pmatrix} 1 & 0 & 0 \\ 0 & -0.5 & 0 \\ 0 & 0 & -0.5 \end{pmatrix}\mathrm{d}\varepsilon^{\mathrm{pl}}_{xx} - \frac{2}{3}\gamma_i\chi_i\begin{pmatrix} 1 & 0 & 0 \\ 0 & -0.5 & 0 \\ 0 & 0 & -0.5 \end{pmatrix}|\mathrm{d}\varepsilon^{\mathrm{pl}}_{xx}| \tag{10}$$

Rearranging Equation (10), the expression governing the dynamic of each backstress component, according to the CKH model for a uniaxial loading case, can eventually be obtained in Equation (11).

$$\mathrm{d}\chi_i = C_i\mathrm{d}\varepsilon^{\mathrm{pl}}_{xx} - \gamma_i\chi_i|\mathrm{d}\varepsilon^{\mathrm{pl}}_{xx}| \tag{11}$$

2.2. Mathematical Formalization of B-W Model

The conventional B-W model is described by four equations, as in (12), according to the studies conducted by Bouc [34] and Wen [35]. The model considers x and $\dot{x}$ as inputs and Y and z as outputs.

$$\begin{cases} Y = Y_2(z + Y_1) \\ Y_2 = b^{cx} \\ Y_1 = k_1 x + k_2\mathrm{sign}(x)x^2 + k_3 x^3 \\ \dot{z} = \dot{x}(\alpha - (\gamma + \beta\mathrm{sign}(\dot{x})\mathrm{sign}(z))z^n) \end{cases} \tag{12}$$

The last differential equation in (12) represents the evolution of the hysteretic variable z, which allows for one to replicate the amplitude of the hysteresis cycle. The variable Y_1 is

described with a polynomial function similar to a nonlinear spring, the second equation is an exponential function, and all the equations, from the second to the fourth, included in Equation (12), are combined in the first one. Observing the last equation of (12) the time dependence can easily be eliminated and an equivalent form is then provided in Equation (13):

$$\mathrm{d}z = \mathrm{d}x(\alpha - (\gamma + \beta \mathrm{sign}(\mathrm{d}x)\mathrm{sign}(z))\,z^n) \tag{13}$$

This equation (13) can be further improved, as in (14), by considering another parameter δ, which allows for one to emphasize the asymmetry in the width of the hysteresis cycle as described in [43].

$$\mathrm{d}z = \mathrm{d}x((\alpha + \delta x) - (\gamma + \beta \mathrm{sign}(\mathrm{d}x)\mathrm{sign}(z))\,z^n) \tag{14}$$

After reconsidering the Bouc–Wen model used in our case, the inputs are the total strain (ε_{xx}) and the sign of its differential $(\mathrm{d}\varepsilon_{xx})$, while the output is the stress along the loading direction (σ_{xx}).

3. Materials and Methods

3.1. Experimental Data

The material involved in this work was 42NiCrMo4 quenched and tempered steel. The technical drawing of the plain specimen engaged to perform both strain-controlled tests and stress-controlled test is shown in Figure 1, where dimensions and tolerances are reported. The experimental data were sampled with a frequency of 10 Hz, and the strain-rate was approximately $\pm 2.5 \times 10^{-3}\,\mathrm{s}^{-1}$. The yield and the ultimate strengths, extracted from the tensile test performed according to ASTM E8/E8M-11 [45], are $S_Y = 500\,\mathrm{MPa}$ and $S_U = 700\,\mathrm{MPa}$, respectively. R_ε is defined as the ratio between the minimum and the maximum imposed total strain during the strain-controlled test. Regarding the strain-controlled tests performed at $R_\varepsilon \approx -1$, the sampling was continuous due to the relatively low number of cycles, whereas, during the strain-controlled test executed at $R_\varepsilon \neq -1$, the sampling was carried out by blocks, as the number of cycles was much higher.
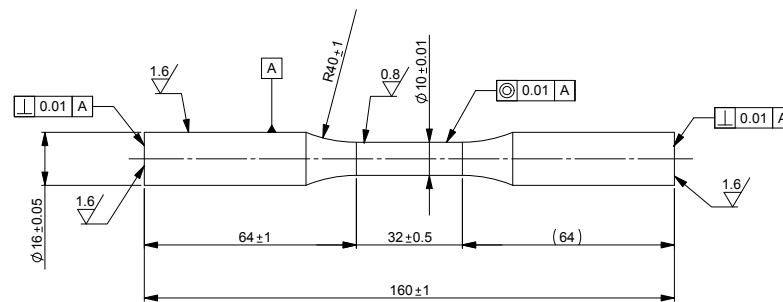
Figure 1. Technical drawing of the specimen used to perform both strain-controlled tests and stress-controlled test.

The choise of material investigated in this study does not represent any limitation to the proposed procedure, as no hypothesis about the material was introduced during the procedure and the CIKH model is generally engaged to model the plasticity of metals. The proposed technique can be extended to any metal with a sufficient ductile behaviour. Three strain-controlled tests and one stress-controlled test were performed on plain specimens. Two of the strain-controlled tests were conducted at $R_\varepsilon \approx -1$ and are shown in Figure 2, where the stabilized cycles are indicated in red (Cycle I and Cycle II), while the rest of the loading history is indicated in grey. Some useful experimental data about the stabilized cycles Cycle I and Cycle II, which are needed to determine the constants of the CKH model, are reported in Table 1. The extreme stress values of the stabilized cycles of strain-controlled tests are indicated with $\sigma_{\max}^{\mathrm{stab}}$ and $\sigma_{\min}^{\mathrm{stab}}$.
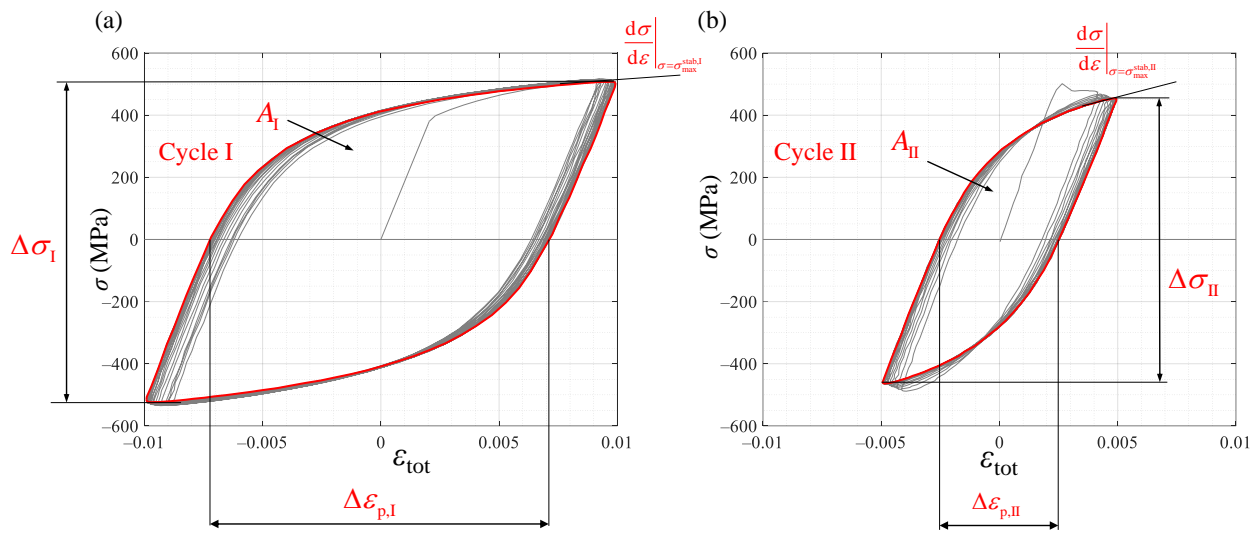
Figure 2. Strain-controlled tests performed at $R_\varepsilon \approx -1$: (**a**) loading I, (**b**) loading II.

Table 1. Useful experimental data extracted from Cycle I and Cycle II.

Stabilized Cycle	$\Delta\varepsilon_p$	$\Delta\sigma$ (MPa)	A (mJ/mm^3)	$\left.\frac{d\sigma}{d\varepsilon_p}\right|_{\sigma=\sigma_{max}^{stab}}$ (GPa)
Cycle I	1.43%	1.03×10^3	12.0	5.81
Cycle II	0.50%	918	3.61	20.2

In Figure 3a, a qualitative trend for a stress-controlled test on a plain specimen is reported in the σ-ε_p coordinates, and the meaningful experimental inputs regarding the stress-controlled test are indicated. The red line in Figure 3a indicates an open ratcheting cycle, which ranges from the maximum plastic strain of cycle N to the minimum plastic strain, and then again reaches the maximum plastic strain of cycle $N + 1$.
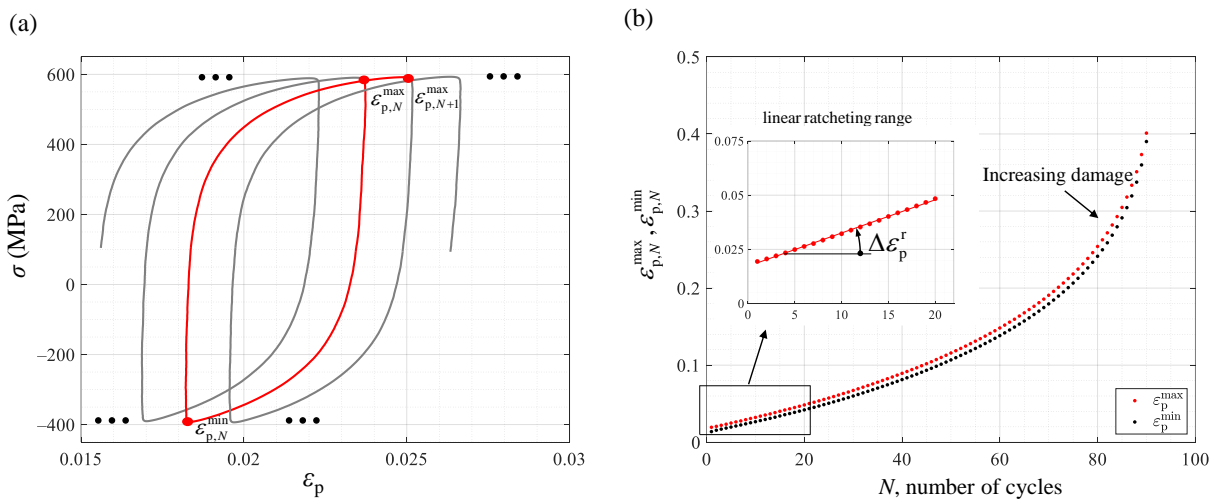

Figure 3. (**a**) Example of a stress-controlled test for a plain specimen with meaningful quantities reported; (**b**) experimental trend of the maximum and minimum plastic strain per cycle of the stress-controlled test involved in the work.

Using the experimental inputs from the stress-controlled test, two important quantities for further analysis are defined in Equations (15) and (16).

$$\Delta\varepsilon_{p,N}^a = \frac{\varepsilon_{p,N+1}^{max} + \varepsilon_{p,N}^{max}}{2} - \varepsilon_{p,N}^{min} \tag{15}$$

$$\Delta\varepsilon_{\mathrm{p},N}^{\mathrm{s}} = \frac{\varepsilon_{\mathrm{p},N+1}^{\max} - \varepsilon_{\mathrm{p},N}^{\max}}{2} \tag{16}$$

Superscripts "s" and "a" stand for shift and amplitude, respectively. These quantities are, in principle, not constant, but numerical simulations using the Chaboche model suggested that $\Delta\varepsilon_{\mathrm{p},N}^{\mathrm{a}}$ and $\Delta\varepsilon_{\mathrm{p},N}^{\mathrm{s}}$ are always asymptotically stable. According to Refs. [46–48], a constant ratcheting rate was reported after an initial settling phase; therefore, $\Delta\varepsilon_{\mathrm{p},N}^{\mathrm{a}}$ can be replaced with $\Delta\varepsilon_{\mathrm{p}}^{\mathrm{a}}$ in Equation (15), and $\Delta\varepsilon_{\mathrm{p},N}^{\mathrm{s}}$ can be replaced with $\Delta\varepsilon_{\mathrm{p}}^{\mathrm{s}}$ in (16). The experimental ratcheting rate, extracted from the stress-controlled test conducted at $R \approx -0.66$, is shown in Figure 3b, where the maximum and minimum plastic strain per cycle are reported. The determination of $\Delta\varepsilon_{\mathrm{p}}^{\mathrm{a}}$ and $\Delta\varepsilon_{\mathrm{p}}^{\mathrm{s}}$, to employ them in the computation of the model parameters, must be carried out by considering that the CKH model cannot reproduce the final part of the graphic in Figure 3b, unless the damage in the model was included so that only the "linear" part of Figure 3b was considered. This zone was taken from approximately the second cycle of the loading until the twentieth, and this is indicated in Figure 3b.

3.2. Efficient Procedure to Calculate CKH Parameters

In this work, a CKH model with three backstress components was considered, and the dynamics of each component, according to our procedure for a qualitative loading with $R_{\varepsilon_{\mathrm{p}}} = 0$, are explained in Figure 4, where the stabilized cycles are indicated in red. $R_{\varepsilon_{\mathrm{p}}}$ is defined as the ratio between the minimum and maximum imposed plastic strain during the plastic strain-controlled test. γ_1 was taken as the highest gamma value, so the first backstress has a rapid dynamic. As shown in Figure 4a, this is responsible for the hysteresis area of the stabilized cycle of the plastic strain-controlled test. γ_2 was modeled as being much lower than γ_1, and the trend of the second backstress is shown in Figure 4b. Its contribution to the hysteresis area of the stabilized cycle is almost null. γ_3 was imposed as exactly null; thus, according to Equation (11), the third backstress evolves linearly, as in Figure 4c. Note that the quantity of the x-axis of Figure 4 is the plastic strain, since the numerical simulations were plastic-strain-controlled. This last situation is experimentally challenging, and the experimental tests are always strain-controlled. As explained in [49], all the expressions shown in the rest of the paper regarding suggested procedure to identify CKH parameters, which were, in principle, obtained from plastic-strain-controlled tests, were generalized to strain-controlled tests without loss of meaning.
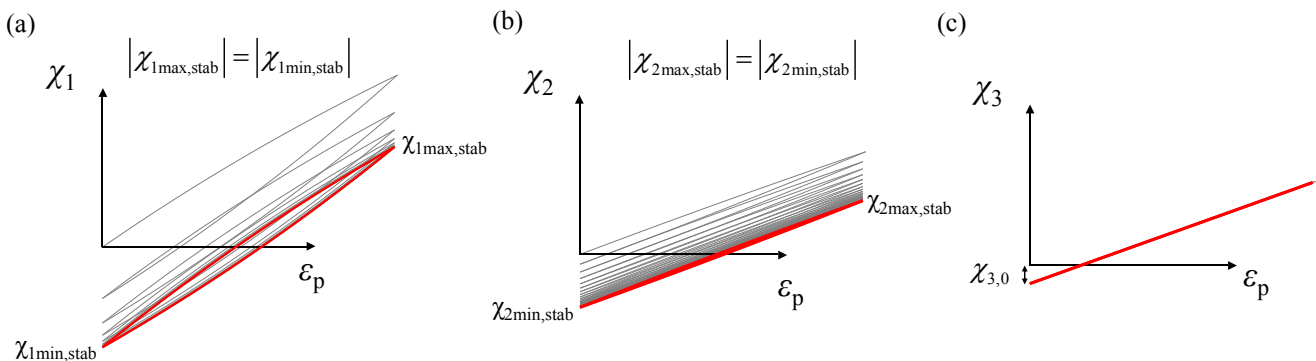
Figure 4. Qualitative explanation of the behaviour of each backstress component according to the proposed procedure: (**a**) rapid backstress, (**b**) slow backstress, (**c**) linear backstress.

To calculate CKH constants, the procedure of [49] is briefly recalled. The values of C_3 and $\chi_{3,0}$ were first determined using the stabilized cycles of strain-controlled tests executed

at $R_\varepsilon \approx -1$ and $R_\varepsilon \neq -1$. The linear system that must be solved is Equation (17), where $\sigma_m \left(\sigma_m = \frac{\sigma_{max} + \sigma_{min}}{2} \right)$ and $\varepsilon_{p,m} \left(\varepsilon_{p,m} = \frac{\varepsilon_{p,max} + \varepsilon_{p,min}}{2} \right)$ are the experimental inputs.

$$\begin{cases} \chi_{3,0} + C_3 \varepsilon_{p,m,I} = \sigma_{m,I} \\ \chi_{3,0} + C_3 \varepsilon_{p,m,II} = \sigma_{m,II} \end{cases} \tag{17}$$

Equations (18)–(20), used to model the global properties of the stabilized cycles of strain-controlled tests, have a general meaning and, in this case, they were all applied to the loadings performed at $R_\varepsilon \approx -1$. C_2 and C_1 were determined as a function of γ_1, using the slope at the inversion points of the experimental stabilized cycles of strain-controlled tests. Assuming $\gamma_2 \Delta \varepsilon_p \ll 1$, which is reasonable considering the low value of γ_2, the nonlinear system (18) was obtained.

$$\begin{cases} C_1 \left(1 - \tanh\left(\frac{\gamma 1 \Delta \varepsilon_{p,I}}{2} \right) \right) + C_2 = -C_3 + \frac{d\sigma}{d\varepsilon_p} \Big|_{\sigma = \sigma_{max}^{stab,I}} \\ C_1 \left(1 - \tanh\left(\frac{\gamma 1 \Delta \varepsilon_{p,II}}{2} \right) \right) + C_2 = -C_3 + \frac{d\sigma}{d\varepsilon_p} \Big|_{\sigma = \sigma_{max}^{stab,II}} \end{cases} \tag{18}$$

In Equation (18), the values of $\frac{d\sigma}{d\varepsilon_p} \Big|_{\sigma = \sigma_{max}^{stab}}$ and $\Delta \varepsilon_p$ are the experimental inputs. The elastic limit was also determined as a function of γ_1, in Equation (19), again assuming $\gamma_2 \Delta \varepsilon_p \ll 1$.

$$\begin{cases} \sigma_{L,I} = \frac{\Delta \sigma_I}{2} - \frac{C_1}{\gamma_1} \tanh\left(\frac{\gamma_1 \Delta \varepsilon_{p,I}}{2} \right) - \frac{C_2 + C_3}{2} \Delta \varepsilon_{p,I} \\ \sigma_{L,II} = \frac{\Delta \sigma_{II}}{2} - \frac{C_1}{\gamma_1} \tanh\left(\frac{\gamma_1 \Delta \varepsilon_{p,II}}{2} \right) - \frac{C_2 + C_3}{2} \Delta \varepsilon_{p,II} \end{cases} \tag{19}$$

In Equation (19), the experimental inputs are $\Delta \sigma$ and $\Delta \varepsilon_p$ and, in principle, $\sigma_{L,I}$ and $\sigma_{L,II}$ should be coincident. As this does not occur in practice, but the value of the elastic limit is unique for the material, it was defined as $\sigma_L = \frac{\sigma_{L,I} + \sigma_{L,II}}{2}$. The last useful property of the stabilized cycle of the strain-controlled test is the hysteresis area, which was modeled, depending on γ_1 and assuming $\gamma_2 \Delta \varepsilon_p \ll 1$, as in Equation (20) for Cycle I and Cycle II, respectively.

$$\begin{cases} A_I^{mod} = 2 \sigma_L \Delta \varepsilon_{p,I} + 2 \left(\frac{C_1}{\gamma_1} \Delta \varepsilon_{p,I} - 2 \frac{C_1}{\gamma_1^2} \tanh\left(\frac{\gamma_1 \Delta \varepsilon_{p,I}}{2} \right) \right) \\ A_{II}^{mod} = 2 \sigma_L \Delta \varepsilon_{p,II} + 2 \left(\frac{C_1}{\gamma_1} \Delta \varepsilon_{p,II} - 2 \frac{C_1}{\gamma_1^2} \tanh\left(\frac{\gamma_1 \Delta \varepsilon_{p,II}}{2} \right) \right) \end{cases} \tag{20}$$

The experimental inputs in these latter two equations are the same as those brought into play during elastic limit computation. Different error functions were then introduced:

- An error function that quantifies the discrepancy between the elastic limits deduced from the two independent cycles:
  $\Sigma = \left| \frac{\sigma_{L,I} - \sigma_{L,II}}{\sigma_L} \right|$
- The relative error function on the prediction of the hysteresis area of cycle I:
  $\Lambda_I = \frac{A_I^{mod} - A_I}{A_I}$
- The relative error function on the prediction of the hysteresis area of cycle II:
  $\Lambda_{II} = \frac{A_{II}^{mod} - A_{II}}{A_{II}}$

These three functions were combined into a global error function defined in (21):

$$\psi(\gamma_1) = (1 - \alpha)\Sigma^2 + \alpha \left(\Lambda_1^2 + \Lambda_2^2 \right) \tag{21}$$

where α can balance the importance of considering the hysteresis area of the stabilized cycle of strain-controlled tests rather than the amplitude of the stabilized cycle of strain-controlled tests, or vice versa, and the value of α is imposed in the range $[0, 1]$. After obtaining the

value of γ_1 that minimized the global error function in (21), which is indicated with a red arrow in Figure 5, C_1, C_2 and σ_L were updated following Equations (18) and (19). A qualitative graphic of the global error function (21) for different values of α is reported in Figure 5.
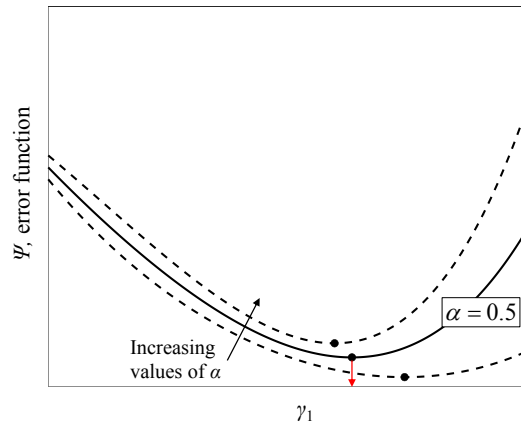

Figure 5. Qualitative trend of $\psi(\gamma_1)$ for different values of α.

To calculate the value of γ_2 the stress-controlled test was exploited and the experimental ratcheting rate was involved. Considering a CKH model with two backstress components, the relationship between σ_m and $\Delta\varepsilon_p^a$ and $\Delta\varepsilon_p^r$ is provided in Equation (22), in accordance with [49].

$$\sigma_m = \sum_{i=1}^{2} \frac{C_i}{\gamma_i} \frac{\sinh\left(\gamma_i \Delta\varepsilon_p^r / 2\right)}{\sinh\left(\gamma_i \Delta\varepsilon_p^a\right)} \tag{22}$$

As, generally, $\gamma_i \Delta\varepsilon_p^r \ll 1$ for each backstress component due to the small plastic strain increment per cycle, a simplified form of Equation (22) was used, as in Equation (23).

$$\sigma_m = \frac{\Delta\varepsilon_p^r}{2} \sum_{i=1}^{2} \frac{C_i}{\sinh\left(\gamma_i \Delta\varepsilon_p^a\right)} \tag{23}$$

After obtaining γ_1, Equation (23) can easily be inverted and γ_2 can be found. It is interesting to highlight that, according to Equation (22), plastic shakedown $\left(\Delta\varepsilon_p^r = 0\right)$ can occur only for null values of the average stress. The superscript of the sum in Equation (23) is 2, but the model involved in the work employed three backstress components. The maximum value of the third backstress component, due to its linear trend, evolves cycle per cycle, as in Equation (24).

$$\chi_{3,\,i+1}^{max} = \chi_{3,\,i}^{max} + C_3 \Delta\varepsilon_p^r \tag{24}$$

According to Equation (24), it is clear that the only achievable equilibrium, according to the CKH with three backstress components, is given by $\Delta\varepsilon_p^r = 0$, which means that only plastic shakedown can occur as equilibrium. Therefore, $\Delta\varepsilon_p^a$ and $\Delta\varepsilon_p^r$ cannot be considered constant anymore. In Figure 4, it is qualitatively shown, according to the full demonstration in [49], that the maximum and the minimum values of the first and second backstress components are exactly opposite for the stabilized cycle of a strain-controlled test. This last statement can be further extended to stress-controlled tests [49]. The average stress of the stabilized cycle of the stress-controlled test can be related to its corresponding average

plastic strain, similarly to Equation (17), and the average plastic strain value of the stabilized cycle is formalized in Equation (25).

$$\varepsilon_{\mathrm{p}}^{\mathrm{m}} = \frac{\sigma_{\mathrm{m}} - \chi_{3,0}}{C_3} \tag{25}$$

If the value of C_3 is high, then the average plastic strain of the stabilized cycle is low, and can be reached after few cycles. Despite this, by exploiting a fully relaxed stabilized cycle arising from a test at $R_\varepsilon \neq -1$, the obtained value of C_3 is generally smaller than the values of C_1 and C_2; due to this, a certain number of cycles are needed to reach the plastic shakedown. Therefore, $\Delta_{\mathrm{p}}^{\mathrm{a}}$ and $\Delta\varepsilon_{\mathrm{p}}^{\mathrm{r}}$ can still be considered constant without any loss of accuracy, and Equation (23) continues to be a valid expression to calculate the value of γ_2. The determination of the parameters of the CKH model with three backstess components, according to the proposed procedure, is finally resumed in the steps below:

- The determination of C_3 and $\chi_{3,0}$, extracted from the average stress and average plastic strain of the experimental stabilized cycles of two strain-controlled tests;
- The slope at the inversion points was used to determine C_1 and C_2;
- The elastic limit was computed as the average of the elastic limit of Cycle I and Cycle II, exploiting the stress amplitude and plastic strain amplitude of the stabilized cycles of strain-controlled tests;
- The hysteresis areas of the stabilized cycles I and II were modeled and used the same experimental inputs as the elastic limit computation;
- Three error functions based on the elastic limit and the hysteresis area of the stabilized cycle I and II were introduced and combined in a global error function (21);
- The value of γ_1 was found to be that which minimized the global error function (21), and C_1, C_2 and σ_{L} were then updated following Equations (18) and (19);
- γ_2 was the last parameter to be computed by exploiting the experimental ratcheting rate and according to Equation (23).

The first step considered one strain-controlled test executed at $R_\varepsilon \neq -1$ and one at $R_\varepsilon \approx -1$ (Loading II). From the second to the last steps, the two strain-controlled tests realized at $R_\varepsilon \approx -1$ were considered. The last step involved the stress-controlled test.

The use of three strain-controlled tests and one stress-controlled test allows to achieve an equal number of unknown parameters and equations. However, this combination of tests is not strictly necessary. In fact, according to [49], two strain-controlled tests with different amplitudes and different mean points, of the stabilized cycles, plus one stress-controlled test, is enough to calculate the parameters. In this study, as explained later, the strain-controlled test performed at $R_\varepsilon \neq -1$ did not have a consistent hysteresis area of the stabilized cycle, and so was only engaged to calculate the values of C_3 and $\chi_{3,0}$.

3.3. Algorithm to Calculate B-W Parameters

The determination of the parameters of the B-W model was carried out using the command `lsqnonlin` of Matlab Software [50]. This provides a nonlinear least squares fit, and various algorithms can be used. In this case, the L-M algorithm was employed. To briefly explain this algorithm, consider a nonlinear system, as in (26), where vector q gathers the variables of the problem.

$$\Psi_{\mathrm{d}} = Q(q) \tag{26}$$

Ψ_{d} indicates the desirable configuration and $J(q)$ indicates the Jacobian of the vectorial function $Q(q)$ obtained as $J(q) = \frac{\partial Q}{\partial q}$. The problem can be solved with an iterative procedure in which a linear approximation from the step i to $i+1$ is assumed as in Equation (27).

$$Q(q_{\mathrm{i}} + \zeta) = Q(q_{\mathrm{i}}) + J\zeta \tag{27}$$

The value of ζ at each step was determined by using the L-M iterative technique, which consists of a linear system solution, as shown in Equation (28).

$$(J^{t}J + \lambda I)\zeta = J^{t}(\Psi_{d} - Q(q_{i})) \qquad (28)$$

In the linear system, (28) λ is a powerful leverage, which allows for one to obtain different method behaviours: for low values of λ, the algorithm tends toward the Newton–Raphson method, whereas for high values of λ, it tends toward the gradient method. The possibility of varying the value of λ during the iteration allows for one to prefer the gradient method next to the singularities, while Newton–Raphson method lacks accuracy, while far from singularities, the Newton–Raphson method is preferred because it converges to the solution more quickly than the gradient method. In our case, B-W constants were determined to minimize the difference between the computed output and the experimental output.
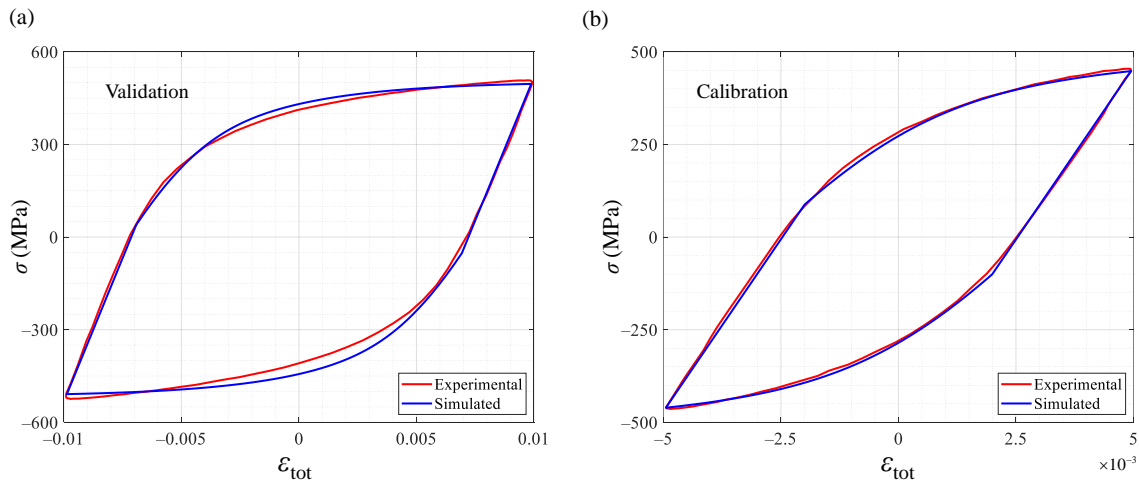
4. Results and Validation

In the first part of this section, the results obtained through pointwise fitting are exposed. In the middle part, firstly, the stabilized cycles of the strain-controlled tests and the ratcheting rate of the stress-controlled test are reproduced by exploiting the calculated coefficients according to the proposed procedure for the CKH model with three backstress components. Then, the improvements due to the introduction of the fourth backstress are exposed, and the outcomes of the calculation of Voce isotropic hardening law parameters are shown. In the final part of the section, the results obtained through the Bouc–Wen model are presented.

4.1. Determination of CKH with Pointwise Fitting

The determination of CKH parameters was also carried out using a pointwise fitting between the experimental data represented by the stabilized cycles of the strain-controlled tests performed at $R_{\varepsilon} \approx -1$ and the modeled curve obtained by Equation (9) and Equation (11), with three backstress components imposing $\gamma_3 = 0$. The fitting was conducted on cycle I, then validated on cycle II and vice versa. For this operation, the Matlab software was employed and the command `fit` [50] was engaged, which provides a nonlinear least squares fit with the default Matlab algorithm. The results are shown in Figures 6 and 7.
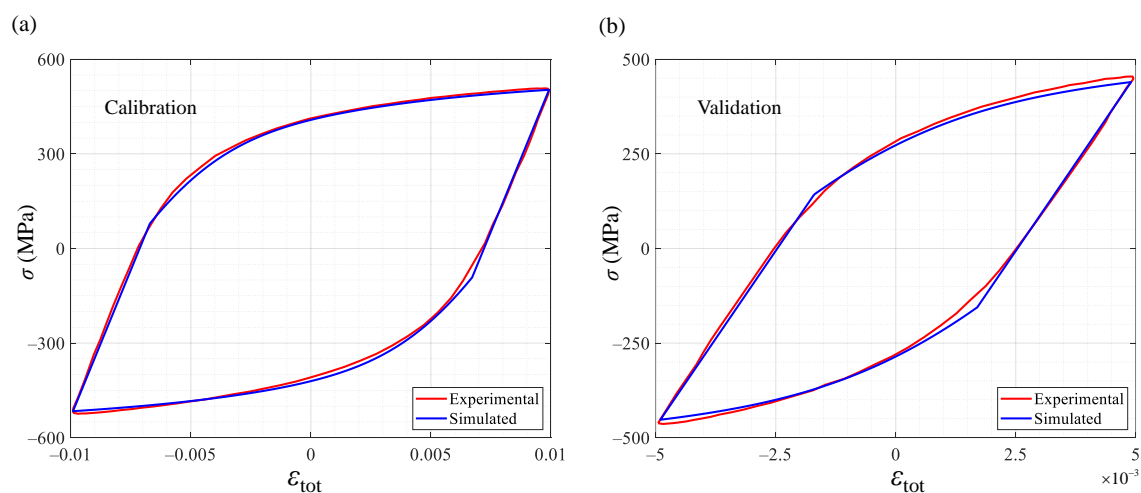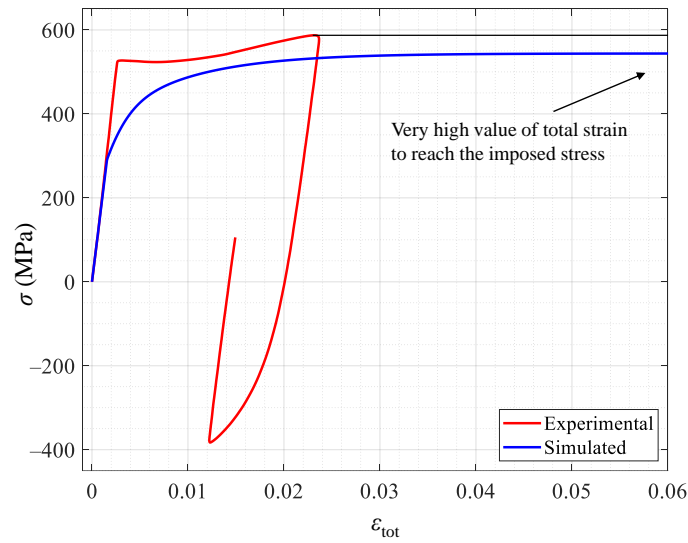

Figure 6. Comparisons between experimental and modeled stabilized cycles of strain-controlled tests using a pointwise fitting: (**a**) cycle I, used for calibration, (**b**) cycle II, used for validation

(a)

(b)

Figure 7. Comparisons between experimental and modeled stabilized cycles of strain-controlled tests using a pointwise fitting: (**a**) cycle I, used for validation, (**b**) cycle II, used for calibration

Considering Figure 6, whose results present a better forecast than those of Figure 7, the ratcheting was validated with the parameters obtained from the first computation. In this case, an in-depth discussion should occur regarding the validation of the stress-controlled test. Starting from Equation (11), the evolution of the nonlinear backstress components can be obtained, as in Equation (29).

$$\begin{cases} \chi_i = \frac{C_i}{\gamma_i} + (\chi_{i,0} - \frac{C_i}{\gamma_i})\exp(-\gamma_i(\varepsilon_p - \varepsilon_{p,0}) \quad \text{if} \quad \varepsilon_p - \varepsilon_{p,0} > 0 \\ \chi_i = -\frac{C_i}{\gamma_i} + (\chi_{i,0} + \frac{C_i}{\gamma_i})\exp(-\gamma_i(\varepsilon_{p,0} - \varepsilon_p) \quad \text{if} \quad \varepsilon_{p,0} - \varepsilon_p > 0 \end{cases} \tag{29}$$

The maximum value of the first of Equation (29) is given by $\lim_{\varepsilon_p \to \infty} \chi_i = \chi_i^{\max} = \frac{C_i}{\gamma_i}$, whereas the minimum value of the second of Equation (29) is given by $\lim_{\varepsilon_p \to -\infty} \chi_i = \chi_i^{\min} = -\frac{C_i}{\gamma_i}$. Some other considerations are needed to analyze the linear backstress, where the maximum and the minimum value reached during the entire cycle loading are provided by $\chi_3^{\max} = \chi_{3,0} + C_3\left(\varepsilon_p^{\max} - \varepsilon_{p,0}\right)$ and $\chi_3^{\min} = \chi_{3,0} + C_3\left(\varepsilon_p^{\min} - \varepsilon_{p,0}\right)$, respectively. Recalling Equation (9), the maximum and the minimum values of the stress obtained during the cyclic loading can be expressed by $\sigma_{xx}^{\max} = \sigma_0 + \chi_1^{\max} + \chi_2^{\max} + \chi_3^{\max}$ and $\sigma_{xx}^{\min} = -\sigma_0 + \chi_1^{\min} + \chi_2^{\min} + \chi_3^{\min}$, respectively. It is clear that once the parameters are obtained from the fitting, the values of $\chi_1^{\max}$, $\chi_2^{\max}$, $\chi_1^{\min}$ and $\chi_2^{\min}$ can be determined. Regarding stress-controlled tests, the values obtained from $\sigma_0 + \chi_1^{\max} + \chi_2^{\max}$ and from $\sigma_0 + \chi_1^{\min} + \chi_2^{\min}$ are far from the maximum and the minimum values of the imposed stress, and can only be reached by exploiting the third backstess. Depending on the values of C_3 and $\chi_{3,0}$, these can be obtained at very high plastic strain values. In Figure 8, a piece of the first modeled ramp of the stress-controlled test is shown. The parameters used to reproduce the blue curve in Figure 8 were those obtained by fitting Cycle I. At reasonable total strain values for the first ramp, a flat zone is observed; this means that, due to the parameter values obtained from the fitting, the first and the second backstress components immediately saturate to values that are not high enough to reach the maximum value of the imposed stress. The third backstress, due to the low values of C_3 and $\chi_{3,0}$ obtained from the fit, cannot contribute to the total modeled stress for "low" total strain values. As a consequence, only very high total strain values, then very high plastic strain values, could allow for the total stress to reach the target. This last point has no physical meaning, and nothing would change by using the parameters obtained by fitting Cycle II, given that, as shown in Table 2, the values of C_3 and $\chi_{3,0}$ are still too low.

The values of Chaboche parameters obtained with a pointwise fitting are reported in Table 2.
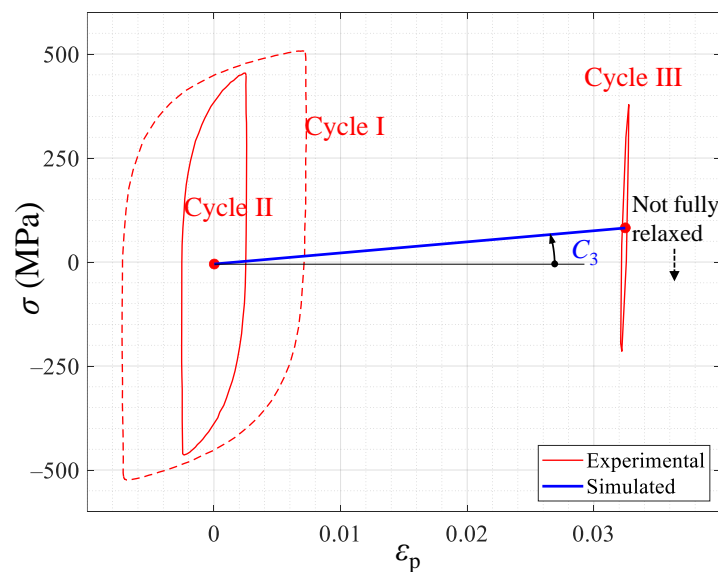
Figure 8. Comparison between the experimental first ramp of stress-controlled test and the modeled first ramp of stress-controlled test through the coefficients obtained with the pointwise fitting.

Table 2. Numerical values of CKH model parameters obtained with the pointwise fitting.

Extracted From	C_1 (MPa)	γ_1	C_2 (MPa)	γ_2	C_3 (MPa)	$\chi_{3,0}$ (MPa)	σ_L (MPa)
Cycle I	78.23×10^3	677	16.68×10^3	122	0.463	-6.46	298
Cycle II	114.7×10^3	971	28.55×10^3	245	0.017	-6.35	274

4.2. Validations of the Proposed Procedure with Three Backstresses

The results obtained according to Equation (17) are summarized in Figure 9, where the stabilized cycle of the loading conducted at $R_\varepsilon \neq -1$ is shown and, together with Cycle II, this was used to calculate the values of C_3 and $\chi_{3,0}$. In Figure 9, the experimental midpoints of the stabilized cycles satisfy the linear trend of the third backstress component, and it is also important to highlight that the stabilized cycle of the strain-controlled test performed at $R_\varepsilon \neq -1$ may be not fully relaxed.


Figure 9. $C_{3,0}$ and $\chi_{3,0}$ to predict the relationship between the mean plastic strain of the stabilized cycle and mean stress of the stabilized cycle.

In Figure 10, comparisons between the experimental and the simulated stabilized cycles executed at $R_\varepsilon \approx -1$ are reported. The simulated curves were reproduced by parameters C_1, C_2, γ_1, γ_2, C_3 and $\chi_{3,0}$ obtained with Equations (17)–(21). The simulated models tend to not properly reproduce the zone near the elastic limit, especially in Figure 10b.

(a)

(b)
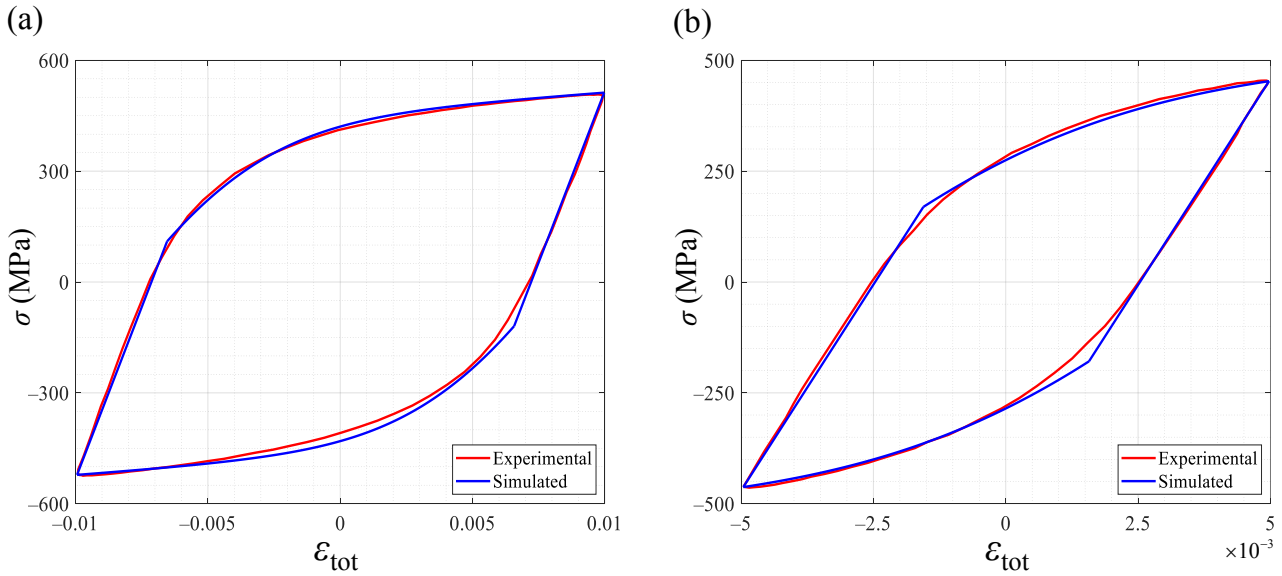
Figure 10. Comparisons between the experimental and simulated stabilized cycles using the suggested procedure: (**a**) Cycle I, (**b**) Cycle II.

The determination of γ_2 and the corresponding validation of the ratcheting rate need a particular focus. The experimental strain-controlled test conducted at $R_\varepsilon \neq -1$ is not fully relaxed, and this means that a high value of C_3 resulted from the proposed procedure. If the value of C_3 is high, then the modeled average plastic strain of the stabilized cycle is low, and can be reached after few cycles, resulting in an early plastic shakedown. This could not allow one for one to reproduce the linear trend of Figure 3b, given that Equation (23) is still not accurate enough to compute the value of γ_2. Nevertheless, to show that the procedure can reproduce the ratcheting-rate, the value of C_3 can be set as equal to 0 and its value, obtained from the proposed procedure, can be switched to C_2, obtaining a final value of C_2, which is $C_2' = C_2 + C_3$. The results are then reported in Figure 11.

(a)

(b)
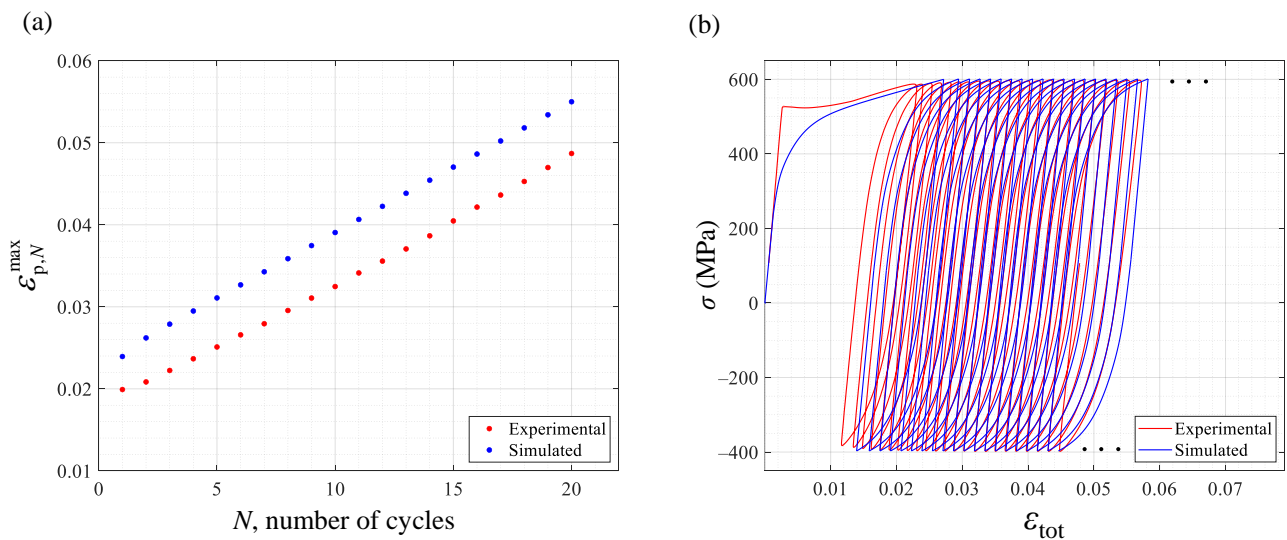
Figure 11. (**a**) Comparison between the experimental and simulated ratcheting rate using the proposed procedure, (**b**) a comparison between the experimental and simulated stress-controlled loading cycles.

The values of CKH parameters obtained following the proposed procedure are presented in Table 3.

Table 3. Parameters obtained following the proposed procedure for CKH model with three backstress components.

C_1 (MPa)	γ_1	C_2 (MPa)	γ_2	C_3 (MPa)	$\chi_{3,0}$ (MPa)	σ_L (MPa)
69.21×10^3	426	2.836×10^3	4.63	2.669×10^3	-4.86	316

4.3. Introduction of the Fourth Backstress

To better reproduce the zone near the elastic limit, a fourth backstress, which is more rapid than the first, was added and calibrated on Cycle II. In Figure 12, ε_B and ε_D indicate the strains that correspond to the elastic limit for the modeled curve; then, $\varepsilon_A = \varepsilon_B$, $\varepsilon_C = \varepsilon_D$, $\sigma_A \neq \sigma_B$ and $\sigma_C \neq \sigma_D$. After a high value of γ_4 was imposed, the aim was to find the ratio of C_4 and γ_4, which minimized the error function defined in (30). This is equal to the imposition of a coincident point A with point B, and point C with point D, in Figure 12.

$$\varphi\left(\frac{C4}{\gamma_4}\right) = |\sigma_A - \sigma_B|^2 + |\sigma_C - \sigma_D|^2 \tag{30}$$

After the introduction of the fourth backstress, the value of σ_L must be updated according to Equation (19); thus, the value of σ_L' is ultimately given by (31)

$$\sigma_L' = \sigma_L - \frac{C_4}{\gamma_4} \tag{31}$$

Another interesting consideration about the evolution of the modeled hysteresis area of the stabilized cycle of strain-controlled tests, due to the introduction of the fourth backstress, is explained in Figure 13a where the hysteresis area decreases with the increasing value of $\frac{C_4}{\gamma_4}$. Observing Equation (20) and updating the value of σ_L following (31), it is evident that the area must decrease. Nevertheless, the prediction of the cycle amplitude, provided by Equation (19), remains unchanged because of the high value of γ_4. In Figure 13b, a comparison between the experimental Cycle II and its modelling is shown. Dashed line was obtained through the procedure with the three backstress components, while the solid line was obtained by adding the fourth backstress component. Figure 13b highlights the improvement provided by the fourth backstress near the elastic limit zone.
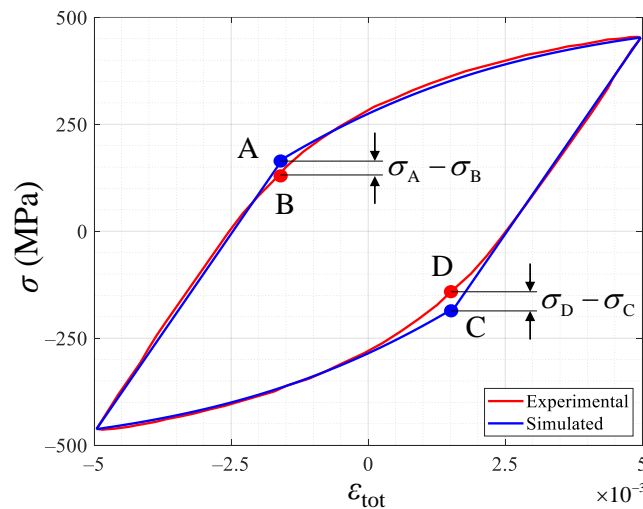

Figure 12. Graphical explanation of the procedure used to introduce the fourth backstress component.
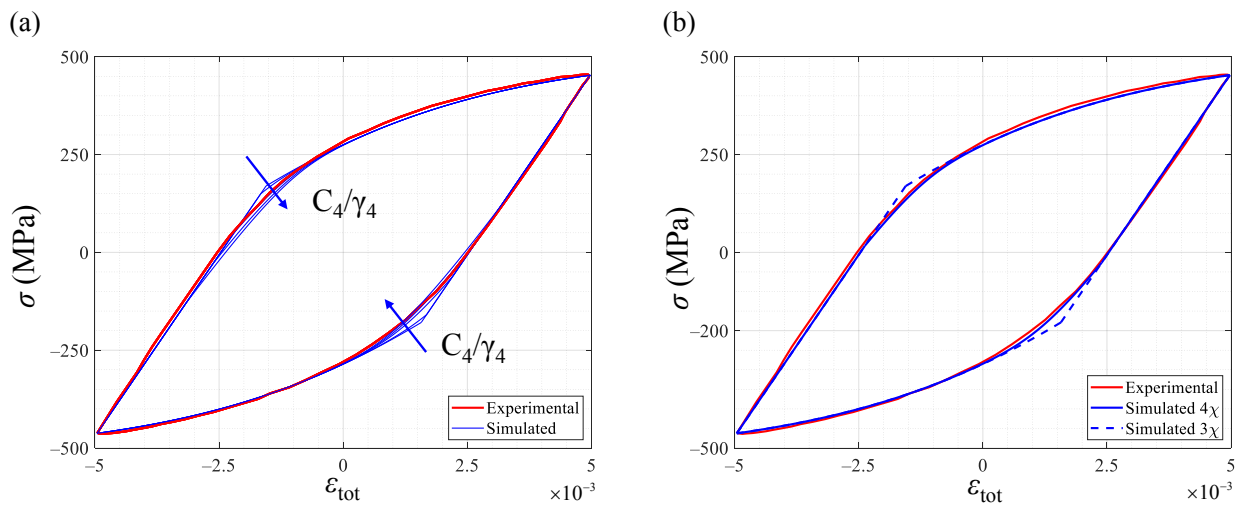
Figure 13. (**a**) Evolution of the modeled hysteresis area of stabilized cycle with respect to a change in $\frac{C_4}{\gamma_4}$, (**b**) improvements in the prediction near the elastic limit for Cycle II by adding the fourth backstress component.

Definitive comparisons between the simulated stabilized cycles (with four backstress components) and the experimental stabilized cycles of strain-controlled tests performed at $R_\varepsilon \approx -1$ and $R_\varepsilon \neq -1$, are shown in Figure 14.
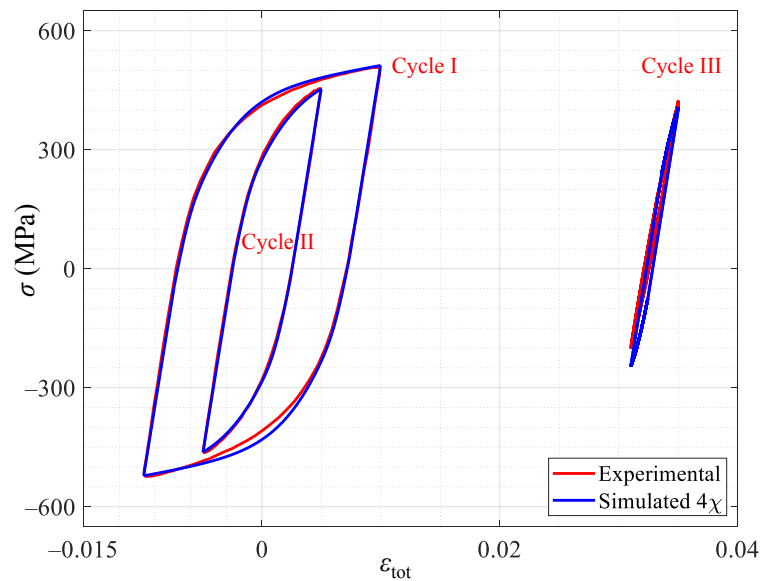
Figure 14. Comparisons between the experimental and simulated stabilized cycles after adding the fourth backstress component for Cycle I, Cycle II and Cycle III.

The addition of the fourth backstress did not change the constant values reported in Table 3, except for the new elastic limit σ_L'. The numerical values of the parameters are all gathered in Table 4.

Table 4. Numerical values of the parameters obtained by following the proposed procedure for CKH model with four backstress components

C_1 (MPa)	γ_1	C_2 (MPa)	γ_2	C_3 (MPa)	$\chi_{3,0}$ (MPa)	σ_L' (MPa)	C_4 (MPa)	γ_4
69.21×10^3	426	2.836×10^3	4.63	2.669×10^3	-4.86	240	381.8×10^3	5×10^3

It is worth noting that, in Ref. [24], where a successive trial-and-error continuous optimisation approach, using the Matlab software, was engaged to calculate the parameters, some differences can be highlighted with respect to the values shown in Table 4. In particular, in [24], a model with three backstress components was employed, but the value of γ_3 was not assumed to be null. This was the lowest of the γ values, but still much higher than the value of γ_2 obtained through the procedure proposed in this work. In [8], an optimization algorithm based on the Newton trust region method and an accumulated true strain term was exploited to calculate the parameters for CIKH with two backstress components. The obtained γ_2 value was much higher than that obtained through the procedure proposed in this study. In Ref. [3], a pointwise fitting was performed and the obtained value of γ_2 was still much higher than that obtained through the proposed procedure. In sum, clear differences regarding the values of γ_2 were obtained using the proposed procedure with respect to the classical approaches available in the literature.

4.4. Isotropic Hardening

A well-known fact is that the the elastic limit initially depends on the cumulated plastic strain; thus, an isotropic hardening model (Voce) was introduced to account for this phenomenon. The exponential istropic hardening rule of Voce is formalized in Equation (32), where Q and b are the equation parameters and p is the same as in Equation (6). σ_0 corresponds to the elastic limit when $p = 0$.

$$\sigma_Y = \sigma_0 + Q(1 - \exp(-bp)) \tag{32}$$

For high values of the cumulated plastic strain $(p \to \infty)$, Equation (33) provides a relationship between the constant value of the elastic limit of the CKH model and Voce's equation.

$$\sigma_L = \sigma_0 + Q \tag{33}$$

The transient during the initial cycles, as shown in Figure 15, ending at the stabilized Cycle II, was used to find the value of Q and b. In particular, the maximum stress value at the inversion points is described by Equation (34), whereas the minimum stress value is given by Equation (35).

$$\sigma_N^{\max} = \sum_{i=1}^{4} \chi_{i,N}^{\max} + \sigma_Y(p) \tag{34}$$

$$\sigma_N^{\min} = \sum_{i=1}^{4} \chi_{i,N}^{\min} - \sigma_Y(p) \tag{35}$$

By substituting Equation (33) in Equation (32), Equation (36) can be obtained. σ_Y is the experimental input found by exploiting Equations (34) and (35); therefore, the values of Q and b were obtained through a least-squares fit of Equation (36).

$$\sigma_Y - \sigma_L = -Q \exp(-bp) \tag{36}$$

The result of the least-squares fit operation is then resumed in Figure 16, where a comparison between the experimental data and the best-fit curve is provided.

The numerical values of the constants of Voce istropic hardening model are reported in Table 5. There were no differences between those obtained for CIKH model with three backstress components and those obtained with four backstress components except for the value of σ_0.
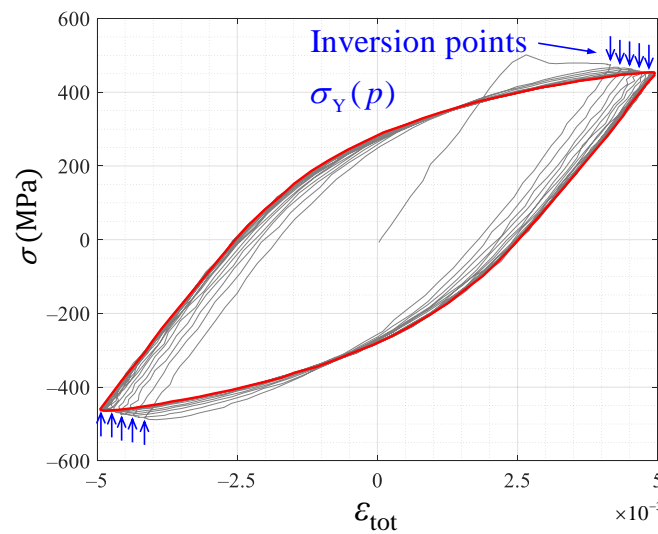
Figure 15. Cycle II transient used to calculate the parameters of the Voce model by exploiting the stress values at the inversion points.
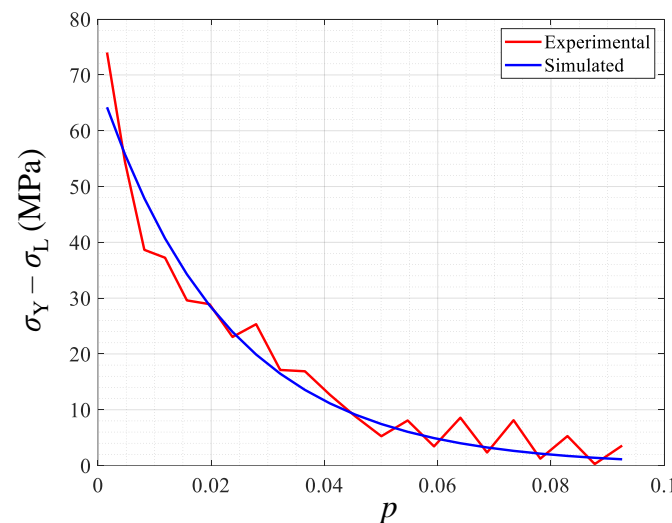

Figure 16. Best-fit curve and experimental data that can predict the trend in the elastic limit.

Table 5. Numerical values of the parameters of Voce isotropic hardening model.

| Model	σ_0 (MPa)	Q (MPa)	b
3 backstress	385	−69	44.5
4 backstress	309	−69	44.5

4.5. Results of B-W Model

In this section, the B-W model's ability to predict cyclic plasticity is presented. The parameter values were obtained using the entire first cyclic loading, tested at $R_\varepsilon \approx -1$; then, cycle II was validated, and vice versa. After this, the stress-controlled test was also used to obtain the values of B-W parameters, and cycle I and cycle II were employed for validation. In the case of the stress-controlled test, considering what is stated in Section 3.1, only a few initial cycles (from the second to the fifth) were considered. The ability of the B-W model to predict the stabilized cycles of strain-controlled tests is shown in Figures 17–19, whereas in Figure 20, the stress-controlled test and its corresponding modeled trend is presented.
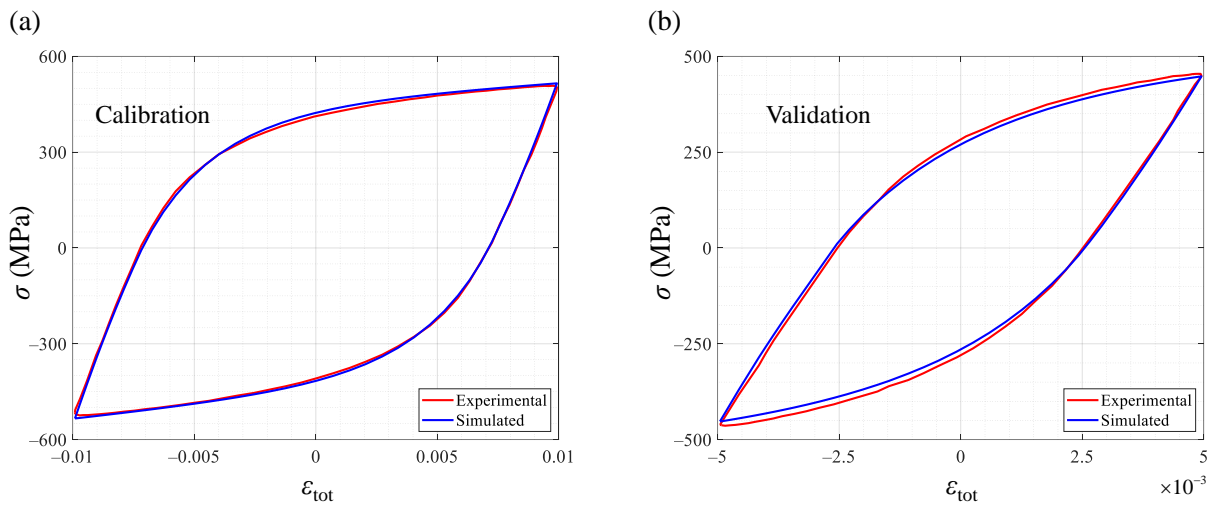
Figure 17. Comparisons between the experimental and modeled stabilized cycles of strain-controlled tests using B-W model: (**a**) cyclic loading I, used for calibration, (**b**) cycle II, used for validation.
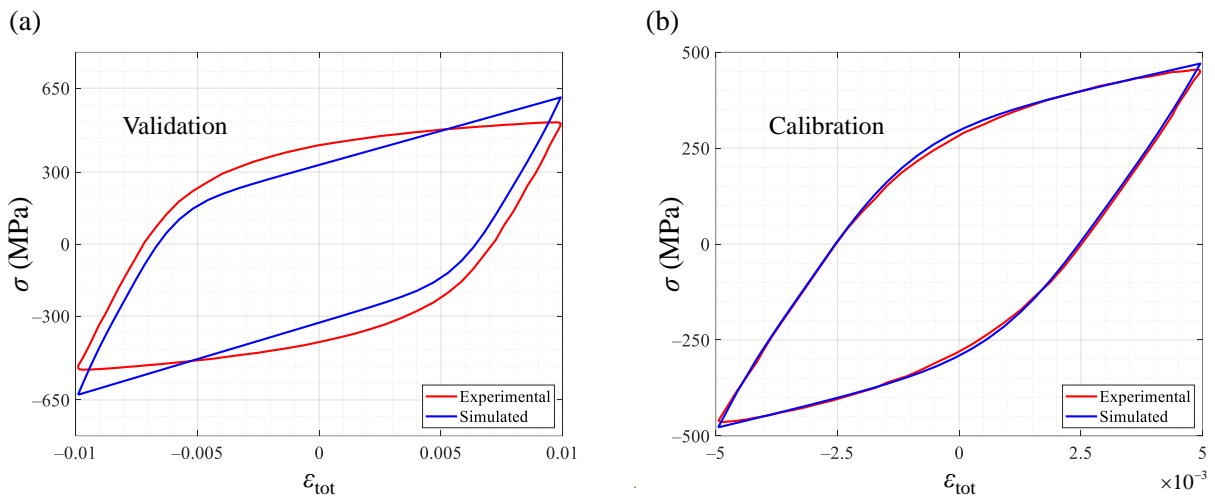
Figure 18. Comparisons between experimental and modeled stabilized cycles of strain-controlled tests using B-W model: (**a**) cycle I, used for validation, (**b**) cyclic loading II, used for calibration.
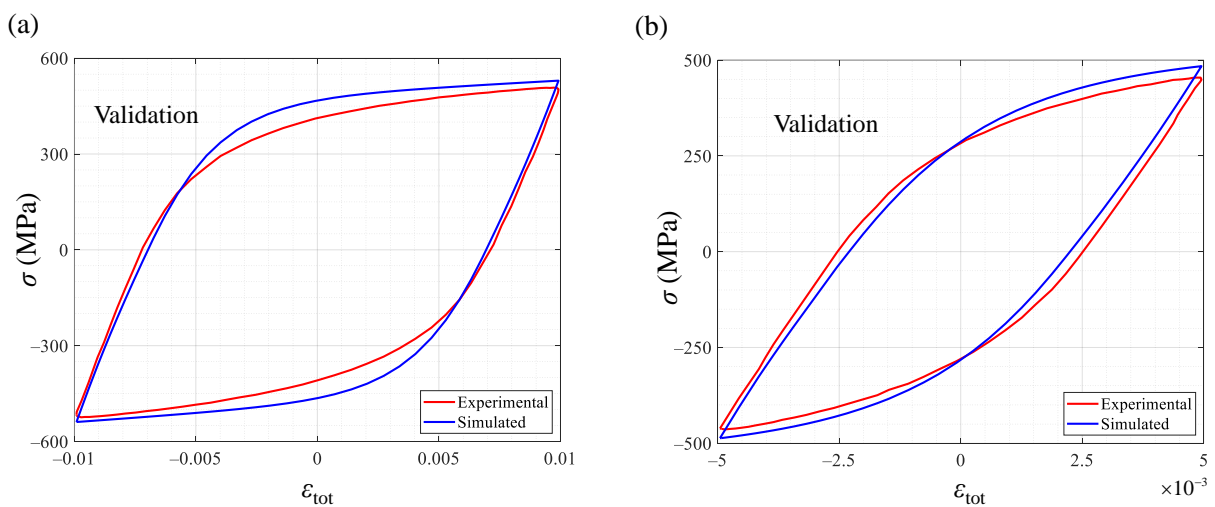
Figure 19. Comparisons between experimental and modeled stabilized cycles of strain-controlled tests using B-W model: (**a**) cycle I, used for validation, (**b**) cycle II, used for validation. The stress-controlled test was involved in calibration.
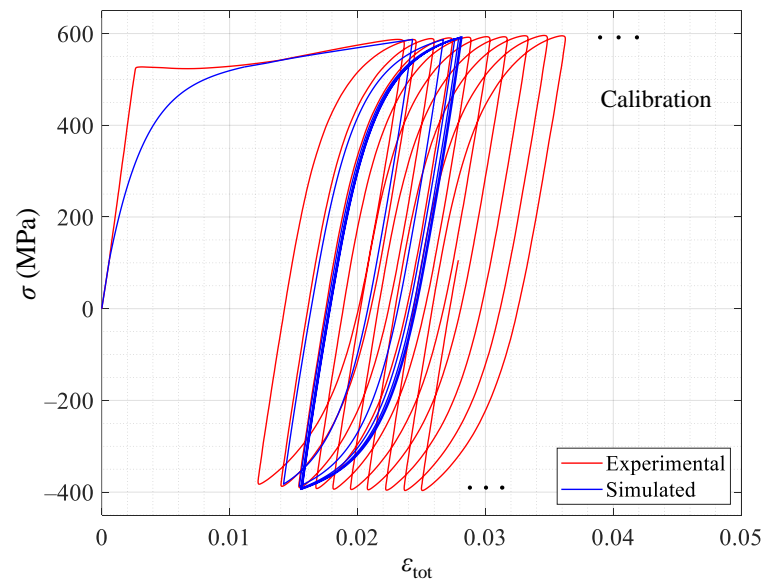
Figure 20. Stress-controlled test used for calibration of B-W model parameters with its corresponding modeled trend.

The numerical values of the B-W model parameters obtained for the three different cases are summarized in Table 6.

Table 6. Obtained values for the parameters of B-W model.

Extracted From	α (MPa)	β (MPa^{1-n})	γ (MPa^{1-n})	n	δ (MPa)	c	k_1 (MPa)	k_2 (MPa)	k_3 (MPa)
Strain-controlled test I	15.4	0.391	0.184	0.858	−0.041	0	0.674	0	0
Strain-controlled test II	14.7	0.011	0.005	1.940	−0.086	0	2.94	0	0
Stress-controlled test	15.5	0.068	0.036	1.290	−0.026	0	0.479	0	0

5. Conclusions

In this work, we used a novel procedure to identify CIKH model parameters. Three strain-controlled tests and one stress-controlled test were used to implement the procedure. Two strain-controlled tests were performed at $R_\varepsilon \approx -1$, whereas the third one was conducted at $R_\varepsilon \neq -1$. From the strain-controlled tests, we extracted the stabilized cycles (Cycle I and Cycle II for the strain-controlled tests performed at $R_\varepsilon \approx -1$ and Cycle III for the strain-controlled test executed at $R_\varepsilon \neq -1$), and we determined the global properties of the stabilized cycles, namely, the slope at the inversion points, the hysteresis area, the stress amplitude, the average stress and the average plastic strain. The experimental stress-controlled test provided the ratcheting rate. The procedure validations are shown in Figures 10 and 11, and an accurate matching can be seen between the modeled curves and the experimental curves. A fourth backstress was added to improve the prediction near the elastic limit, as shown in Figure 14, resulting in a high level of local accuracy. The model was then completed by the determination of the Voce isotropic hardening model parameters, eventually obtaining the CIKH model. A pointwise fitting was used to determine the parameters of the CKH model with three backstress components. Figure 6 can better reproduce the experimental data than Figure 7. This is due to the wider range of experimental total strain, on which the fitting of Figure 6 was developed. However, the parameters obtained by fitting Cycle I cannot reproduce the extreme points of Cycle II, as in Figure 6b, and the numerical values of parameters C_3 and γ_2 are not physically meaningful. Therefore, it was not possible to reproduce the ratcheting rate. The Bouc–Wen model was also considered to reproduce the cyclic plastic behaviour, and the parameters obtained to fit the entire cyclic loading I showed a better ability to reproduce the stabilized cycles of strain-controlled tests than those obtained that fit the entire cyclic loading II and the stress-controlled test. This is shown in Figures 17–19, and is due to the wider range of total

mechanical strain in Cycle I. The parameters of the Bouc–Wen model, obtained by fitting the stress-controlled test, allow for the reproduction of the ratcheting rate, but not at the quality level obtained by following the proposed procedure. To conclude, the proposed procedure to calculate CIKH model parameters is physics-based, and is only formulated on closed-form expressions, which show how the parameters govern each global property. The equations are easily manageable, whereas, when a pointwise fitting is performed, the optimization dynamic behind the software is not fully understandable. The proposed technique involves four experimental cyclic loadings, which are still a reasonable number to determine the model parameters in an efficient way. This last statement allows for one to cover more experimental cases instead of completing the fitting on only one cycle, which clearly results in a good prediction for that cycle but can lack accuracy if validated on a cycle with a different R from that used for the calibration.

Some qualitative expectations about the numerical values of certain parameters of the CIKH model, obtained through the proposed procedure, can be provided. The value of C_1 is expected to be higher than the value of C_2. The value of γ_2 is expected to fall in the range 1–10, or even below this, whereas the value of C_3 is lower than C_1 and C_2. The value of σ_L is expected to be of the same order, but lower than the yield strength obtained through the monotonic test. To eventually improve the zone near the elastic limit, a fourth backstress can be added and a high value of γ_4 is recommended, such as $\gamma_4 \geq 5000$.

The limit of this study is that it is focused on a uniaxial case. However, there are some applications; for example, fatigue analyses of notched components loaded under torsion and so multiaxially, as in [12], where the CKH model parameters were calibrated on the uniaxial loading case according to the proposed procedure, which allowed for accurate fatigue strength predictions to be obtained. Investigations of the calibration techniques used for the determination of CIKH model parameters for multiaxial loading cases can further improve this work. In addition to this, the Bouc–Wen model, according to the results presented in this work, clearly shows the potential to properly describe the cyclic plastic behaviour, apart from the reproduction of the ratcheting rate. This could be an initial basis for finding ways to improve the mathematical form of this model and include an accurate prediction of the ratcheting. However, the application of the B-W model is limited to the uniaxial case, since its mathematical form is only suitable for this case.

Author Contributions: Methodology, C.S., L.R., T.G., L.B. and P.N.; software, C.S., L.R., T.G., L.B. and P.N.; validation, C.S., L.R., T.G., L.B., P.N., L.T., F.C. and L.L.B.; data curation, L.T., F.C. and L.L.B.; resources, L.T., F.C. and L.L.B.; supervision, L.T., F.C. and L.L.B.; writing—review and editing, C.S., L.R., T.G., L.B. and P.N. All authors have read and agreed to the published version of the manuscript.

Data Availability Statement: Data will be made available on request.

Abbreviations

The following abbreviations are used in this manuscript:

CKH	Chaboche kinematic hardening
CIKH	Chaboche isotropic kinematic hardening
B-W	Bouc-Wen
L-M	Levenberg-Marquardt

References

1. Tiwari, A.; Wang, A.; Müser, M.H.; Persson, B.N.J. Contact Mechanics for Solids with Randomly Rough Surfaces and Plasticity. *Lubricants* **2019**, *7*, 90. https://doi.org/10.3390/lubricants7100090.
2. Benedetti, M.; Fontanari, V.; Lütjering, G.; Albrecht, J. The effect of notch plasticity on the behaviour of fatigue cracks emanating from edge-notches in high-strength β-titanium alloys. *Eng. Fract. Mech.* **2008**, *75*, 169–187. https://doi.org/10.1016/j.engfracmech.2007.03.037.

3. Zobec, P.; Klemenc, J. Application of a nonlinear kinematic-isotropic material model for the prediction of residual stress relaxation under a cyclic load. *Int. J. Fatigue* **2021**, *150*, 106290. https://doi.org/10.1016/j.ijfatigue.2021.106290.

4. Bertini, L.; Le Bone, L.; Santus, C.; Chiesi, F.; Tognarelli, L. High Load Ratio Fatigue Strength and Mean Stress Evolution of Quenched and Tempered 42CrMo4 Steel. *J. Mater. Eng. Perform.* **2017**, *26*, 3784–3793. https://doi.org/10.1007/s11665-017-2845-x.

5. Chaboche, J.L. Time-independent constitutive theories for cyclic plasticity. *Int. J. Plast.* **1986**, *2*, 149–188. https://doi.org/10.1016/0749-6419(86)90010-0.

6. Armstrong, P.J.; Frederick, C.O. *A Mathematical Representation of the Multiaxial Bauschinger Effect*; Technical Report C.E.G.B. Report RD/B/N731; Berkeley Nuclear Laboratories: Berkeley, CA, USA, 1966.

7. Voce, E. The relationship between stress and strain for homogeneous deformations. *J. Inst. Met.* **1948**, *74*, 537–562.

8. Petry, A.; Gallo, P.; Remes, H.; Niemelä, A. Optimizing the Voce–Chaboche Model Parameters for Fatigue Life Estimation of Welded Joints in High-Strength Marine Structures. *J. Mar. Sci. Eng.* **2022**, *10*, 818. https://doi.org/10.3390/jmse10060818.

9. Wójcik, M.; Skrzat, A. Identification of Chaboche–Lemaitre combined isotropic–kinematic hardening model parameters assisted by the fuzzy logic analysis. *Acta Mech.* **2021**, *232*, 685–708. https://doi.org/10.1007/s00707-020-02851-z.

10. Zakavi, S.J.; Zehsaz, M.; Eslami, M.R. The ratchetting behavior of pressurized plain pipework subjected to cyclic bending moment with the combined hardening model. *Nucl. Eng. Des.* **2010**, *240*, 726–737. https://doi.org/10.1016/j.nucengdes.2009.12.012.

11. ANSYS, Inc. *ANSYS Mechanical APDL Theory Reference*; Release 15.0; ANSYS: Canonsburg, PA, USA, 2013.

12. Santus, C.; Romanelli, L.; Grossi, T.; Neri, P.; Romoli, L.; Lutey, A.H.A.; Pedranz, M.; Benedetti, M. Torsional-loaded notched specimen fatigue strength prediction based on mode I and mode III critical distances and fracture surface investigations with a 3D optical profilometer. *Int. J. Fatigue* **2022**, *161*, 106913. https://doi.org/10.1016/j.ijfatigue.2022.106913.

13. Benedetti, M.; Berto, F.; Le Bone, L.; Santus, C. A novel Strain-Energy-Density based fatigue criterion accounting for mean stress and plasticity effects on the medium-to-high-cycle uniaxial fatigue strength of plain and notched components. *Int. J. Fatigue* **2020**, *133*, 105397. https://doi.org/10.1016/j.ijfatigue.2019.105397.

14. Peng, Z.; Tian-Yang, L.; Jian-Guo, G.; Fu-Zhen, X.; Filippo, B. A strain energy density based life prediction model for notched components in low cycle fatigue regime. *Int. J. Press. Vessel. Pip.* **2021**, *193*, 104458. https://doi.org/10.1016/j.ijpvp.2021.104458.

15. Song, Z. ; Komvopoulos, K. Contact mechanics analysis of oscillatory sliding of a rigid fractal surface against an elastic–plastic half-space. *Philos. Mag.* **2014**, *94*, 3215–3233. https://doi.org/10.1080/14786435.2014.953618.

16. Guionnet, C. Modeling of Ratchetting in Biaxial Experiments. *ASME J. Eng. Mater. Technol.* **1992**, *114*, 56–62. https://doi.org/10.1115/1.2904141.

17. Chaboche, J.L. On some modifications of kinematic hardening to improve the description of ratchetting effects. *Int. J. Plast.* **1991**, *7*, 661–678. https://doi.org/10.1016/0749-6419(91)90050-9.

18. Shafiqul, B.; Tasnim, H. Anatomy of coupled constitutive models for ratcheting simulation. *Int. J. Plast.* **2000**, *16*, 381–409. https://doi.org/10.1016/S0749-6419(99)00059-5.

19. Chaboche, J.L.; Kanouté, P.; Azzouz, F. Cyclic inelastic constitutive equations and their impact on the fatigue life predictions. *Int. J. Plast.* **2012**, *35*, 44–66. https://doi.org/10.1016/j.ijplas.2012.01.010.

20. Dafalias, Y.F.; Kourousis, K.I.; Saridis, G.J. Multiplicative AF kinematic hardening in plasticity. *Int. J. Solids Struct.* **2008**, *45*, 2861–2880. https://doi.org/10.1016/j.ijsolstr.2008.01.001.

21. Kourousis, K.I.; Dafalias, Y.F. Constitutive modeling of Aluminum Alloy 7050 cyclic mean stress relaxation and ratcheting. *Mech. Res. Commun.* **2013**, *53*, 53–56. https://doi.org/10.1016/j.mechrescom.2013.08.001.

22. Agius, D.; Kajtaz, M.; Kourousis, K.I.; Wallbrink, C.; Hu, W. Optimising the multiplicative AF model parameters for AA7075 cyclic plasticity and fatigue simulation. *Mech. Res. Commun.* **2018**, *90*, 251–260. https://doi.org/10.1108/AEAT-05-2017-0119.

23. Kourousis, K.I.; Dylan, A.; Chun, W.H.; Subic, A. Constitutive Modeling of Additive Manufactured Ti-6Al-4V Cyclic Elastoplastic Behaviour. *Tech. Mech.* **2016**, *36*, 57–72. https://doi.org/10.24352/UB.OVGU-2017-010.

24. Mooney, B.; Agius, D.; Kourousis, K.I. Cyclic Plasticity of the As-Built EOS Maraging Steel: Preliminary Experimental and Computational Results. *Appl. Sci.* **2020**, *10*, 1232. https://doi.org/10.3390/app10041232.

25. Hill, R. A theory of the yielding and plastic flow of anisotropic metals. *Proc. R. Soc. Lond. Ser. A Math. Phys. Sci.* **1948**, *193*, 281–297.

26. Koo, S.; Han, J.; Marimuthu, K.P.; Lee, H. Determination of Chaboche combined hardening parameters with dual backstress for ratcheting evaluation of AISI 52100 bearing steel. *Int. J. Fatigue* **2019**, *122*, 152–163. https://doi.org/10.1016/j.ijfatigue.2019.01.009.

27. Rezaiee-Pajand, M.; Sinaie, S. On the calibration of the Chaboche hardening model and a modified hardening rule for uniaxial ratcheting prediction. *Int. J. Solids Struct.* **2009**, *46*, 3009–3017. https://doi.org/10.1016/j.ijsolstr.2009.04.002.

28. Lee, C.-H.; Do, V.N.V.; Chang, K.-H. Analysis of uniaxial ratcheting behavior and cyclic mean stress relaxation of a duplex stainless steel. *Int. J. Plast.* **2014**, *62*, 17–33. https://doi.org/10.1016/j.ijplas.2014.06.008.

29. Liu, S.; Liang, G.; Yang, Y. A strategy to fast determine Chaboche elasto-plastic model parameters by considering ratcheting. *Int. J. Press. Vessel. Pip.* **2019**, *172*, 251–260. https://doi.org/10.1016/j.ijpvp.2019.01.017.

30. Mahmoudi, A.H; Pezeshki-Najafabadi, S.M; Badnava, H. Parameter determination of Chaboche kinematic hardening model using a multi objective Genetic Algorithm. *Comput. Mater. Sci.* **2011**, *50*, 1114–1122. https://doi.org/10.1016/j.commatsci.2010.11.010.

31. Agius, D.; Kajtaz, M.; Kourousis, K.I.; Wallbrink, C.; Wang, C.H.; Hu, W.; Silva, J. Sensitivity and optimisation of the Chaboche plasticity model parameters in strain-life fatigue predictions. *Mater. Des.* **2017**, *118*, 107–121. https://doi.org/10.1016/j.matdes.2017.01.027.

32. Moslemi, N.; Gol Zardian, M.; Ayob, A.; Redzuan, N.; Rhee, S. Evaluation of Sensitivity and Calibration of the Chaboche Kinematic Hardening Model Parameters for Numerical Ratcheting Simulation. *Appl. Sci.* **2019**, *9*, 2578. https://doi.org/10.3390/app9122578.

33. Pham, Q.T.; Nguyen, D.T. Parameter Identification of Chaboche Model for Aluminum Alloy Sheets Based on Differential Evolution Algorithm. *J. Adv. Eng. Comput.* **2022**, *6*, 224–232. https://doi.org/10.55579/jaec.202263.375.

34. Bouc, R. Forced vibrations of mechanical systems with hysteresis. In Proceedings of the Fourth Conference on Nonlinear Oscillations, Prague, Czech Republic, 5–9 September 1967; Volume 10, pp. 142–149.

35. Wen, Y.K. Method for random vibration of hysteretic systems. *J. Eng. Mech. Am. Soc. Civ. Eng.* **1976**, *102*, 249–263.

36. Carboni, B.; Lacarbonara, W. Nonlinear dynamic characterization of a new hysteretic device: Experiments and computations. *Nonlinear Dyn.* **2016**, *83*, 23–29. https://doi.org/10.1007/s11071-015-2305-9.

37. Fujii, F.; Tatebatake, K.; Morita, K.; Shiinoki, T. A Bouc–Wen Model-Based Compensation of the Frequency-Dependent Hysteresis of a Piezoelectric Actuator Exhibiting Odd Harmonic Oscillation. *Actuators* **2018**, *7*, 37. https://doi.org/10.3390/act7030037.

38. Zhang, Z.; Tian, X.; Ge, X. Dynamic Characteristics of the Bouc–Wen Nonlinear Isolation System. *Appl. Sci.* **2021**, *11*, 6106. https://doi.org/10.3390/app11136106.

39. Ni, Y.Q.; Ko, J.M.; Wong, C.W. Identification of Non-Linear Hysteretic Isolators from Periodic Vibration Tests. *J. Sound Vib.* **1998**, *217*, 737–756. https://doi.org/10.1006/jsvi.1998.1804.

40. Levenberg, K. A Method for the Solution of Certain Problems in Least-Squares. *Q. Appl. Math.* **1944**, *2*, 66–74.

41. Marquardt, D. An Algorithm for Least-squares Estimation of Nonlinear Parameters. *SIAM J. Appl. Math.* **1963**, *11*, 431–441. https://doi.org/10.1137/0111030.

42. Piotr, B.; Robert, Z.; Pawel, C. Parameter identification of Bouc-Wen model for vacuum packed particles based on genetic algorithm. *Arch. Civ. Mech. Eng.* **2019**, *19*, 322–333. https://doi.org/10.1016/j.acme.2018.11.002.

43. Charalampakis, A.E; Koumousis, V.K. Identification of Bouc–Wen hysteretic systems by a hybrid evolutionary algorithm. *J. Sound Vib.* **2008**, *314*, 571–585. https://doi.org/10.1016/j.jsv.2008.01.018.

44. Neri, P.; Holzbauer, J. Experimental Characterization and Numerical Modeling of Wire Rope Isolators. In Proceedings of the Nodycon: Third International Nonlinear Dynamics Conference, Rome, Italy, 18–22 June 2023.

45. *ASTM E8/E8M-11*; Standard Test Methods for Tension Testing of Metallic Materials. ASTM International: West Conshohocken, PA, USA, 2016.

46. Paul, S.K. Effect of anisotropy on ratcheting: An experimental investigation on IFHS steel sheet. *Mater. Sci. Eng.* **2012**, *538*, 349–355. https://doi.org/10.1016/j.msea.2012.01.058.

47. Zhang, B.; Wang, R.; Hu, D.; Jiang, K.; Hao, X.; Mao, J.; Jing, F. 2020. Constitutive modelling of ratcheting behaviour for nickel-based single crystal superalloy under thermomechanical fatigue loading considering microstructure evolution. *Int. J. Fatigue* **2020**, *139*, 105786. https://doi.org/10.1016/j.ijfatigue.2020.105786.

48. Kreethi, R.; Mondal, A.K.; Dutta, K. Ratcheting fatigue behaviour of 42CrMo4 steel under different heat treatment conditions. *Mater. Sci. Eng.* **2017**, *679*, 66–74. https://doi.org/10.1016/j.msea.2016.10.019.

49. Santus, C.; Grossi, T.; Romanelli, L.; Pedranz, M.; Benedetti, M. A computationally fast and accurate procedure for the identification of the Chaboche isotropic-kinematic hardening model parameters based on strain-controlled cycles and asymptotic ratcheting rate. *Int. J. Plast.* **2023**, *160*, 103503. https://doi.org/10.1016/j.ijplas.2022.103503.

50. *MATLAB and Statistics Toolbox Release 2021b*; The MathWorks, Inc.: Natick, MA, USA, 2021.